# Structural and transport properties of La tungstate and its composite with nickel (II) and copper (II) oxides

Nikita Eremeev [a] *, Yulia Bespalko [a], Ekaterina Sadovskaya [a], Tamara Krieger [a], Svetlana Cherepanova [a], Evgeny Suprun [a], Arcady Ishchenko [a], Mikhail Mikhailenko [b], Mikhail Korobeynikov [c], Vladislav Sadykov [a]

**a:** Federal Research Center Boreskov Institute of Catalysis SB RAS, Novosibirsk 630090, Russia
**b:** Institute of Solid State Chemistry and Mechanochemistry SB RAS, Novosibirsk 630128, Russia
**c:** Budker Institute of Nuclear Physics SB RAS, Novosibirsk 630090, Russia
**\*** Corresponding author: yeremeev21@catalysis.ru

## Abstract

La tungstates possessing a high protonic conductivity (~$10^{-4}$ S/cm at 600 °C) are state-of-the-art materials for hydrogen separation membranes. A promising approach in design of new materials for this application is creation of triple-conductive materials on their basis. The current work aims at studying structural, textural and transport properties of $La_{27}W_5O_{55.5-\delta}$ and the composite of $La_{27}W_5O_{55.5-\delta}$ with NiO and CuO obtained via the mechanical activation and sintered either in a furnace or by radiation thermal sintering using electron beam. The oxide material obtained is distorted double fluorite, while the composites consist of $LaNi_{0.8}W_{0.2}O_{3-\delta}$, NiO and CuO phases. As compared to the oxide sintered in furnace, the electron beam sintered $La_{27}W_5O_{55.5-\delta}$ demonstrates a lower occupancy of $24f$ sites by W, higher La:W ratio and larger grain size. Extended defects including grain boundaries are observed in TEM images. $La_{27}W_5O_{55.5-\delta}$ possesses moderate oxygen transport properties (oxygen tracer diffusion coefficient ~$10^{-10}$ cm²/s at 800 °C). Thermogravimetric analysis demonstrates that the materials exhibit the hydration behavior typical of proton conductors. The oxygen mobility is demonstrated to decline in the composites, which can be caused by a lower oxygen mobility of the $LaNi_{0.8}W_{0.2}O_{3-\delta}$ phase compared to the $La_{27}W_5O_{55.5-\delta}$ one and the diffusion hindered by nanoparticles of NiO and CuO. Reduction followed by reoxidation of the composites leads to increasing oxygen diffusivity, which can be related to partial unblocking of fast diffusion pathways.

## Key findings

● $La_{27}W_5O_{55.5}$ are distorted double fluorites, and their composites exhibit complex phase composition.

● E-beam sintering results in decreasing residual porosity, which is promising for fabrication of permselective layers of hydrogen separation membranes.

● $La_{27}W_5O_{55.5}$ demonstrates good hydration ability and moderate oxygen transport properties.

## 1. Introduction

Development of new mixed $O^{2-}/e^-$, $H^+/e^-$ and $H^+/O^{2-}/e^-$ conductive materials has been a relevant problem in design of such devices for modern energy as high-performance permselective membranes [1–5], solid oxide fuel cells [2–6] and electrolyzers [2, 3–5, 7]. A high $H^+$ conductivity is obviously crucial for hydrogen permeable membranes [4, 5, 8–16]. A significant electronic conduc-tivity contribution is required to avoid the limitation of hydrogen transport across the membrane by coupled movement of electrons or holes as well [4, 5, 8, 9, 13, 14]. Using cermet materials comprised of a component with a high protonic conductivity (such as ceramic oxide or solid solution) and a component with a high electronic conductivity (such as metal or metal alloy) has been a promising approach in the design of materials for the hydrogen sepa-

ration membranes [8, 10–12, 17]. In addition, oxide ionic conductivity has been suggested to be high enough to enable proton transport mechanisms involving hydroxyl hops [4, 5, 13, 18, 19]; furthermore, additional yield of hydrogen can be achieved via $H_2O$ splitting occurring along with $O^{2-}$ anion transport across the membrane [1, 4, 5, 14, 15, 20, 21]. Hence, triple-conductive materials should be quite suitable for this application. The following equation can be written for the hydrogen permeation flux ($j(H_2)$) across the triple-conductive membrane (Equation 1):

$$j(\text{H}_2) = \frac{-RT}{8F^2l} \int_{(1)}^{(2)} \sigma_H \cdot \left( \frac{\sigma_O + \sigma_{el}}{\sigma_H + \sigma_O + \sigma_{el}} dlnP(\text{H}_2) \right.$$
$$\left. + \frac{\sigma_O}{\sigma_H + \sigma_O + \sigma_{el}} dlnP(\text{O}_2) \right), \quad (1)$$

where $R$ is universal gas constant; $T$ is temperature; $F$ is Faraday constant; $l$ is membrane thickness; $\sigma_H$, $\sigma_O$ and $\sigma_{el}$ are protonic, oxide-ionic and electronic conductivity, respectively; $P(H_2)$ and $P(O_2)$ are hydrogen and oxygen partial pressure, respectively; indices (1) and (2) represent the partial pressure values at the membrane fuel and purge side compartments, respectively [1, 16].

Ln tungstates and molybdates $Ln_{6-x}MO_{12-\delta}$ (or, more precisely, $Ln_{28-x}M_{4+x}O_{54+3x/2}V_{2-3x/2-\delta}$, where Ln = La, Nd, Ho, Er, Tm, Yb, etc.; M = W, Mo; $V$ is the oxygen vacancy) are oxides possessing fluorite, bixbyite or orthorhombic structure with protonic and oxide ionic conductivity, which may demonstrate a contribution of p- or n-type of conductivity depending on the composition and conditions (temperature, humidity, oxygen partial pressure) as well (total conductivity is ~$1 \cdot 10^{-2}$ S/cm at 600 ºC) [14, 17, 21–32]. La tungstates $La_{6-x}WO_{12-\delta}$ (LWO) considered to be promising proton-conducting membrane materials and electrolytes have been studied in details [1, 15, 21, 22, 24, 26–29, 33–41]. LWO phase stability was demonstrated to be dependent on the La:W ratio. E.g., for the sintering temperature of 1500 ºC, $La_{6-x}WO_{12-\delta}$ oxides are single-phase for the La:W ratio of 5.3–5.7, with this interval narrowing down at lower sintering temperature (e.g. 5.2–5.4 for the sintering temperatures of 1300 ºC) [28]. The ionic conductivity of La tungstates possesses a bell-shape dependence on the La:W ratio determined by the defect structure: variation of content of the oxygen vacancies which can be filled by hydroxyls as proton-containing species in contact with gas hydrogen or water vapors [34, 35]. Hence, $La_{27}W_5O_{55.5-\delta}$ (or, alternatively writing, $La_{5.4}WO_{11-\delta}$) composition seems to provide a compromise between conductivity and phase stability.

The oxide ionic conductivity of La tungstates was generally studied by impedance spectroscopy [38, 39] which gives the information on the overall oxygen mobility, not allowing to elucidate details of oxygen transport mechanisms. However, we can assume that it is possible to distinguish such interesting features of ionic transport in LWO as fast ionic conductivity along grain boundaries and slower conductivity within grain bulk [34]. Moreover, in our previous work [31], according to the studies of oxygen isotope exchange with $C^{18}O_2$ of Ln molybdates $Ln_{10}Mo_2O_{21-\delta}$ (Ln = Nd, Ho), a high oxygen diffusivity along grain boundaries and a lower diffusivity within grain bulk (two-dimensional diffusion) were revealed.

Another problem related to the application of lanthanide tungstates is the requirement to provide their high density while forming defect fluorite or bixbyite polymorphs with a high conductivity, which requires high temperatures (1500–1600 ºC) and long-term (up to 24 h) treatment using conventional sintering in a furnace [25, 28]. Hence, fabrication of functional ceramics based on such materials is a separate problem. A promising approach of solving this problem is radiation thermal sintering (RTS) by a high intensity beam of electrons, enabling conducting synthesis and sintering processes at shorter times and lower temperatures while obtaining less porous products [42–44].

In this work, we studied for the first time the structural, textural and oxygen transport properties and their relationship for $La_{27}W_5O_{55.5-\delta}$ and its composite with NiO and CuO as promising triple-conductive materials for hydrogen separation membranes synthesized by the mechanical activation and radiation-thermal sintering.

## 2. Materials and methods

### 2.1. Synthesis

$La_{27}W_5O_{55.5-\delta}$ (LWO) was synthesized by mechanical activation [30]. Commercially available powders of $La_2O_3$ (VEKTON, 99.999%) were used as the starting materials. $WO_3$ was preliminarily synthesized from tungsten acid (VEKTON, > 98%) by its thermal treatment at 300 ºC. NiO (14.5 wt. %) – CuO (15.5 wt. %) – $La_{27}W_5O_{55.5-\delta}$ (CLWO) composite was synthesized by mechanical activation from NiO, CuO and $La_{27}W_5O_{55.5-\delta}$ powders as described in the work [45]. The synthesis was conducted in an AGO-2 planetary mill (ZAO NOVIC, Russia). It was carried out in stainless steel drums having volume of 150 ml at 1200 rpm rotation rate using $ZrO_2$ balls with diameter of 1 cm. Balls-to-powder weight ratio was 20:1. The process was performed in dry conditions for 20 min for LWO sample and in propanol-2 for 15 min for CLWO sample. The chemical composition of obtained powders was checked repeatedly. According to chemical analysis, Fe impurity content in the powders obtained did not exceed 0.02 wt.%. The powders obtained were calcined at 1100 ºC for 4 h.

For the sample preparation for sintering, dried powders were pressed into pellets. Radiation thermal sintering (RTS) was conducted using an ILU-6 accelerator [46]. Electron energy of 2.4 MeV, pulse beam current of 328 mA and a narrow scan were used. The temperature of the samples was monitored using an S-type thermocouple and a FieldPoint (National Instruments) controlling module. The temperature parameters of the process were set using

accelerator controlling software. The power control was performed by varying pulse repetition frequency, which did not exceed 15 Hz in the experiments. Then the samples were sintered at 1100 ºC for 30 min in the air with the heating and cooling rate of 30 ºC/min.

## 2.2. Characterization

The samples' structural properties were studied by X-ray diffraction (XRD). XRD patterns were acquired by a D8 Advance (Bruker, Germany) diffractometer with Cu Kα monochromatic radiation ($\lambda$ = 1.5418 Å) in $2\theta$ range of 20–90º with the step of 0.05º. The phase composition was determined using PDF-2 and ICSD diffraction databases. The Rietveld refinement was carried out using TOPAS software [47]. Scanning electron microscopy (SEM) and high resolution transmission electron microscopy (HR TEM) images were obtained with a JEM-2010 (Jeol, Japan; lattice resolution 1.4 Å, acceleration voltage 2·105 V) and a Tescan Solaris (The Czech Republic) instruments. Energy-dispersive X-ray spectroscopy (EDX) mapping was carried out using a UltimMAX100 (Oxford, The UK) SDD detector.

Thermogravimetric (TGA) and differential thermal analysis (DTA) techniques were used for the pelletized samples preliminary hydrated in wet air (2 vol.% H2O). The experiments were conducted with using a STA 409 PC "LUXX" thermal analyzer (Netzsch, Germany). The experiments were carried out in dry air flow while cooling from 1000 ºC to room temperature with a ramp of 10 ºC/min for newly synthesized samples and the samples that were kept in water 48 hours and then dried at room temperature.

## 2.3. Oxygen diffusivity studies

The oxygen diffusivity studies were carried out by isotope heteroexchange of oxygen with $C^{18}O_2$ (Supplementary data, Figure S1) and $^{18}O_2$ in a flow reactor using isothermal (IIE) and temperature-programmed (TPIE) modes [48–51]. The samples present in a form of 0.25–0.5 mm granules with a weight of 50 mg were loaded into a tubular quartz reactor with the inner diameter of 3 mm. All the samples were pretreated at 700 ºC for 30 min in the flow of He + 1% O2 (flow rate of 25 ml/min). The composite sample was additionally reduced at 600 ºC for 60 min in the flow of He + 6% H2 (flow rate of 25 ml min$^{-1}$), then reoxidized at 800 ºC for 60 min in the flow of He + 1% CO2 (flow rate of 25 ml/min). IIE experiments were performed at 320 ºC in He + 1% $C^{18}O_2$ (flow rate of 25 ml/min) and at 800 ºC in He + 1% $^{18}O_2$ (flow rate of 25 ml/min). TPIE experiments were carried out in the temperature range of 50–800 ºC with the temperature ramp of 5 ºC/min in He + 1% $C^{18}O_2$ (flow rate of 25 ml/min). The gas composition in the reactor outlet was monitored using SRS 200 and QMS 200 mass spectrometers (Stanford Research Systems, USA) with UGA software. Time (IIE) or temperature (TPIE) dependences of mole fractions of $^{18}O$ atoms ($\alpha$) and $C^{16}O^{18}O$ (or $^{16}O^{18}O$) molecules ($f_{16-18}$) (Figure 1) were investigated

for calculating the oxygen tracer diffusion coefficient ($D^*$) and other oxygen transport characteristics.

## 3. Results and Discussion

### 3.1. Structural features

Figures 2 and 3 demonstrate XRD patterns of the samples. $La_{27}W_5O_{55.5-\delta}$ samples processed conventionally in the furnace (LWO) and using RTS (LWO$_{RT}$) are distorted double fluorites, which is in agreement with the literature data for this composition [21,28,36,39,52,53]. The LWO sample contains insignificant amounts (~ 5 wt.%) of $La_2O_3$ impurity with hexagonal structure, which is typical of the selected La:W ratio and the sintering temperature [23,52], while the LWO$_{RT}$ sample contains $La_6W_2O_{15-\delta}$ admixture with the fluorite structure, which is more typical of lower La:W ratios or higher sintering temperatures [52], and the formation of the $La_6W_2O_{15-\delta}$ admixture may be attributed to the shift in the phase transition temperature toward lower values during RTS in comparison to conventional sintering in a furnace [42–44]. The impurity presence in LWO and LWO$_{RT}$ samples is probably associated with relatively low sintering temperature, since a single-phase sample with ratio La:W = 5.4 can be obtained at the temperature of at least 1300 ºC [28,52]. The Rietveld refinement for the $La_{27}W_5O_{55.5-\delta}$ structure (Figure 4) was carried out using the structural data (ICSD, CC#194092). The unit cell parameter and the occupancy of $24f$ site occupied by La and W ions were refined. The results are given in Table 1.
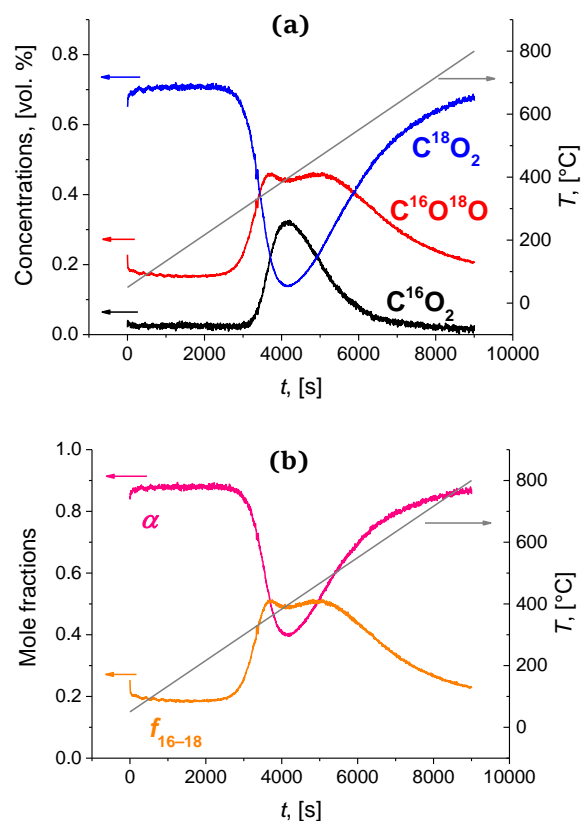


**Figure 1** Concentrations of species (a), and $^{18}O_2$ ($\alpha$) and $C^{16}O^{18}O$ ($f_{16-18}$) fractions in the gas phase (b) during TPIE with $C^{18}O_2$ for LWO sample.

**Table 1** Occupancy of 24*f* site, composition, La:W ratio, unit cell parameter (*a*) and average X-ray scattering region (*D*) for $La_{27}W_5O_{55.5-\delta}$ samples sintered in furnace and by e-beam according to the XRD and Rietveld refinement data.

| Sample | Occupancy of 24*f* | | Composition | | La/W | *a*, [Å] | *D*, [nm] |
|---|---|---|---|---|---|---|---|
| | **La** | **W** | **La** | **W** | | | |
| LWO | 0.92 | 0.08 | 26.08 | 5.92 | 4.41 | 11.1672(2) | 83 |
| LWO$_{RT}$ | 0.96 | 0.04 | 27.04 | 4.96 | 5.45 | 11.1630(2) | 280 |

The 24*f* Wykoff positions are more frequently occupied by W cations for the LWO samples compared to the LWO$_{RT}$ one, which may indicate a different level of structural disordering for these two samples. La:W ratio for the LWO sample is lower than stoichiometric (5.4) apparently due to the $La_2O_3$ phase segregation (Figure 2). La:W ratio for the LWO$_{RT}$ sample is slightly overstoichiometric, which is apparently due to the presence of $La_6W_2O_{15}$ phase with different La:W ratio (3.0). The unit cell parameter *a* of $La_{27}W_5O_{55.5-\delta}$ phase is equal to 11.1672 Å and 11.1630 Å for the conventionally sintered and RTS samples, respectively (Table 1), which indicates a slight contraction of the unit cell after being exposed to the radiation [53]. The average X-ray scattering region size is larger for the LWO$_{RT}$ sample compared to the LWO one sintered at the same temperature (1100 °C). Such an enlargement can be associated with the effects of the electron beam irradiation during RTS, such as stimulated diffusion of ions and increasing sintering rate compared to the conventional sintering [42,53–56]. According to the XRD data, true density calculated from the lattice parameter is 6.65 g/cm³ and 6.66 g/cm³ for the LWO and LWO$_{RT}$ samples, respectively, which is slightly higher compared to the values reported for $La_{27}W_5O_{55.5-\delta}$ in the work [23], probably due to difference in conditions of synthesis and thermal treatment.

The CLWO and CLWO$_{RT}$ composites demonstrate more complex composition than the initial fluorite and nickel (II) – copper (II) oxide phases, apparently due to redistribution of cations during mechanical activation or sintering. The primary phase is identified as orthorhombic perovskite-like $LaNi_{0.8}W_{0.2}O_{3-\delta}$ (LNWO), which is the result of a solid-state reaction between the LWO and NiO phases. The presence of cubic $La_6WO_{12-\delta}$ (in amounts comparable to LNWO) is observed for the CLWO sample but not for the CLWO$_{RT}$ sample, which can be explained by the intensification of solid state reactions during RTS [42–44]. The composite samples also contain cubic bunsenite-like NiO and monoclinic tenorite-like CuO phases (Figures 2 and 3). True density of the CLWO samples can be estimated as 6.6 g/cm³.

### 3.2. Textural characteristics

According to TEM data, large-sized (~100–1000 nm) particles are shown for the LWO sample in agreement with the value of 820 nm estimated using specific surface area and true density values ($d = 3/(S_{sp}\,\rho)$, where *d* is the mean

particle size, $S_{sp}$ and $\rho$ are specific surface area and true density, respectively), and can be explained by relatively high thermal processing temperature (1100 °C).
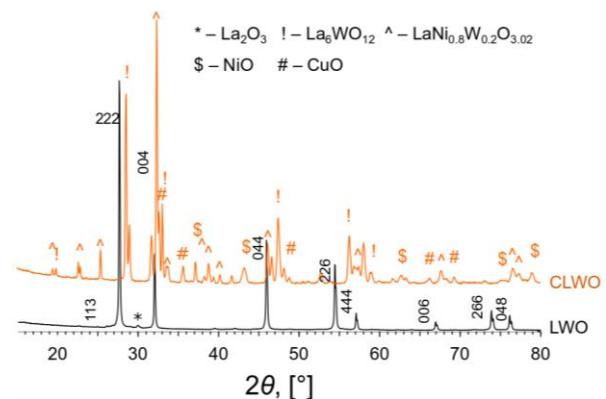


**Figure 2** XRD patterns of $La_{27}W_5O_{55.5-\delta}$ (LWO) and NiO–CuO–$La_{27}W_5O_{55.5-\delta}$ (CLWO) samples sintered conventionally.
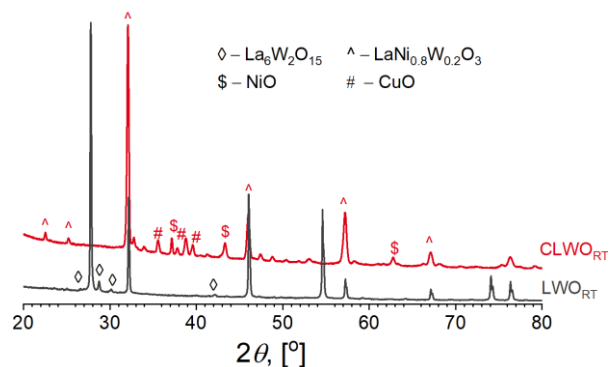


**Figure 3** XRD patterns of the $La_{27}W_5O_{55.5-\delta}$ (LWO$_{RT}$) and NiO–CuO–$La_{27}W_5O_{55.5-\delta}$ (CLWO$_{RT}$) samples sintered by e-beam.
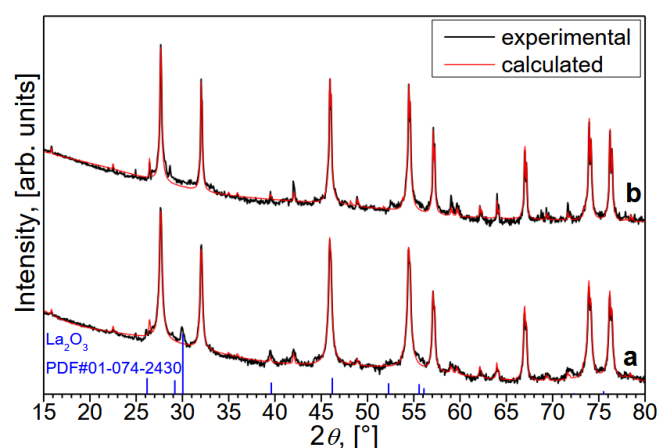


**Figure 4** Rietveld refinement for the $La_{27}W_5O_{55.5-\delta}$ samples sintered at 1100 °C in furnace (a) and by e-beam (b).

La-rich areas apparently related to $La_2O_3$ impurities are demonstrated for the LWO sample, which agrees with the XRD data (Figure 5a). For the LWO$_{RT}$ sample the element distribution is rather uniform (Figure 5b). The pores have an irregular shape; the porosity value can be estimated as ~4%.

Extended defects (e.g., stacking faults, grain boundaries, islet amorphous formations, polycrystalline films on the particles' surface) are detected along with the surface steps and terraces (Figure 6). The grain size is > 100 nm, which agrees with the scattering region size according to XRD. This size is significantly lower compared to the particle size, marking that the samples are polycrystalline; hence, the grain boundary features' effects on the transport properties can be predicted.

Both conventionally and radiation-thermal sintered NiO–CuO–$La_{27}W_5O_{55.5-\delta}$ samples contain pores, but conventionally sintered samples have larger particles compared to the samples after RTS at 1100 °C (Figure 7). A similar trend was demonstrated for lanthanide tungstates and molybdates, bismuth titanates [57, 58]. The extended defects such as grain boundaries are retained for the composites according to the HR TEM data (Figure 8).

### 3.3. Proton content

Figure 9 demonstrates TGA and DTA data for the $La_{27}W_5O_{55.5-\delta}$ sample obtained by RTS. A significant desorption of $H_2O$ is detected for the LWO$_{RT}$ sample. The TGA curve has a shape of three steps, which is typical of such a composition as well as the other proton conductors [23, 32, 59, 60]. Low-temperature desorption (30–300 °C) is associated with elimination of unbound $H_2O$, residual $H_2O$ in pores and physically adsorbed $H_2O$ including water located near surface defects as well [60]. Removal of chemically adsorbed water starts at temperatures >300 °C.

Chemisorbed water is obviously removed at 300–500 °C [60]. Along with this, removal of structural water can start at these temperatures as well [59]. The third step is related to removal of structurally bound water and deprotonation of sample. Complete dehydration of the sample is achieved at 850–900 °C. Proton content in the hydrated sample can be estimated from the overall weight loss as 0.0231 mol ($H^+$)/mol ($O^{2-}$) or 0.649 mol ($H_2O$)/mol (LWO) which means that ~2.3% of all oxygen vacancies are hydrated. This is comparable or even slightly exceeds the values demonstrated for La tungstates with La:W values of 5.2–5.6 [23, 29, 39, 40]. This also suggests a high proton mobility of the La tungstate, which is consistent with the existing literature [22, 41] showing that La tungstate with a similar composition possesses hydrogen tracer diffusion values comparable to the other proton-conducting oxides (Supplementary data, Figure S2) [4, 5, 22, 32, 41, 61–67].
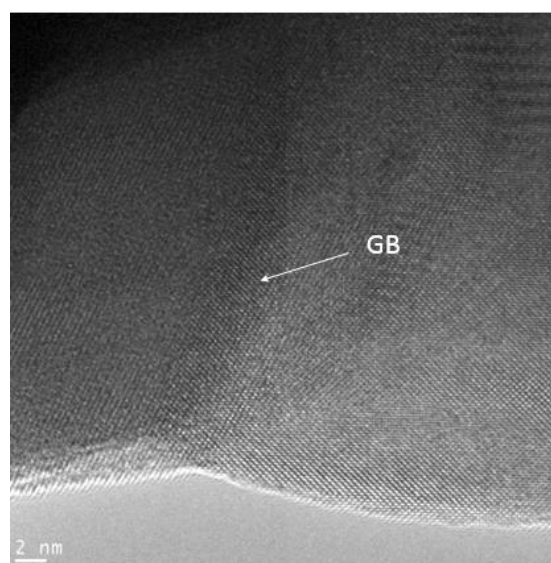


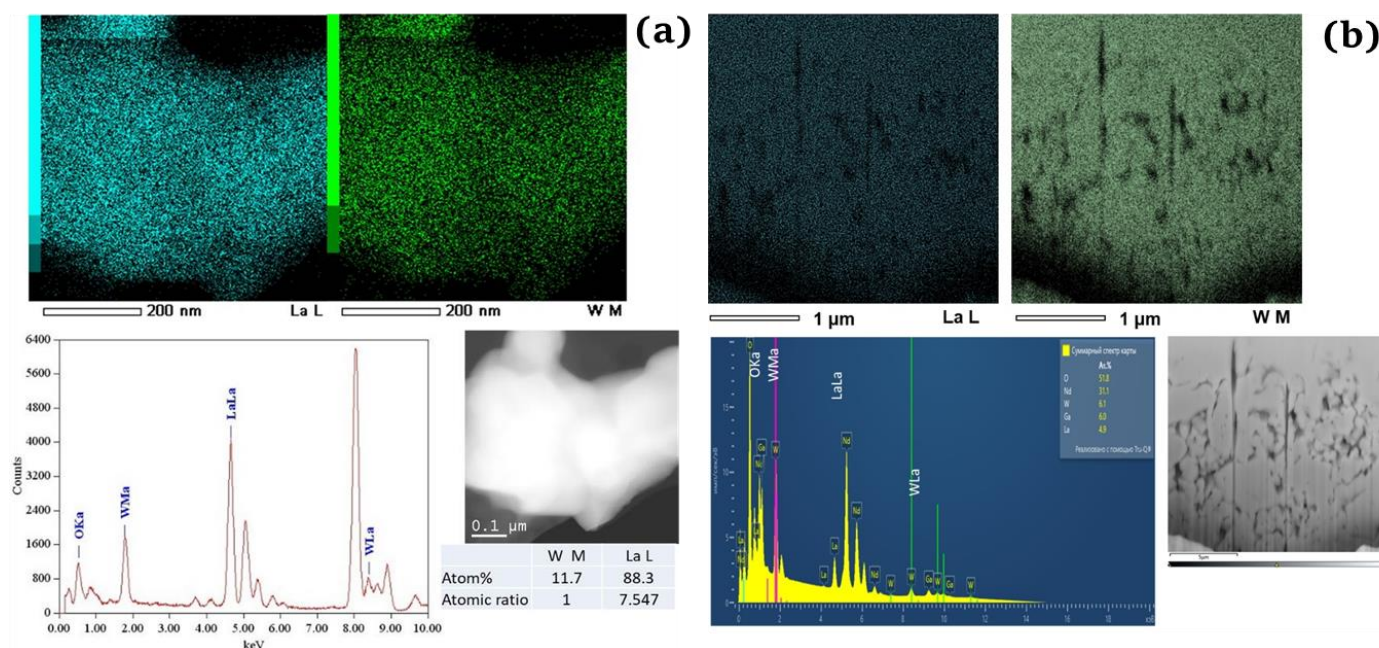**Figure 6** HR TEM image for LWO sample. GB – grain boundaries.



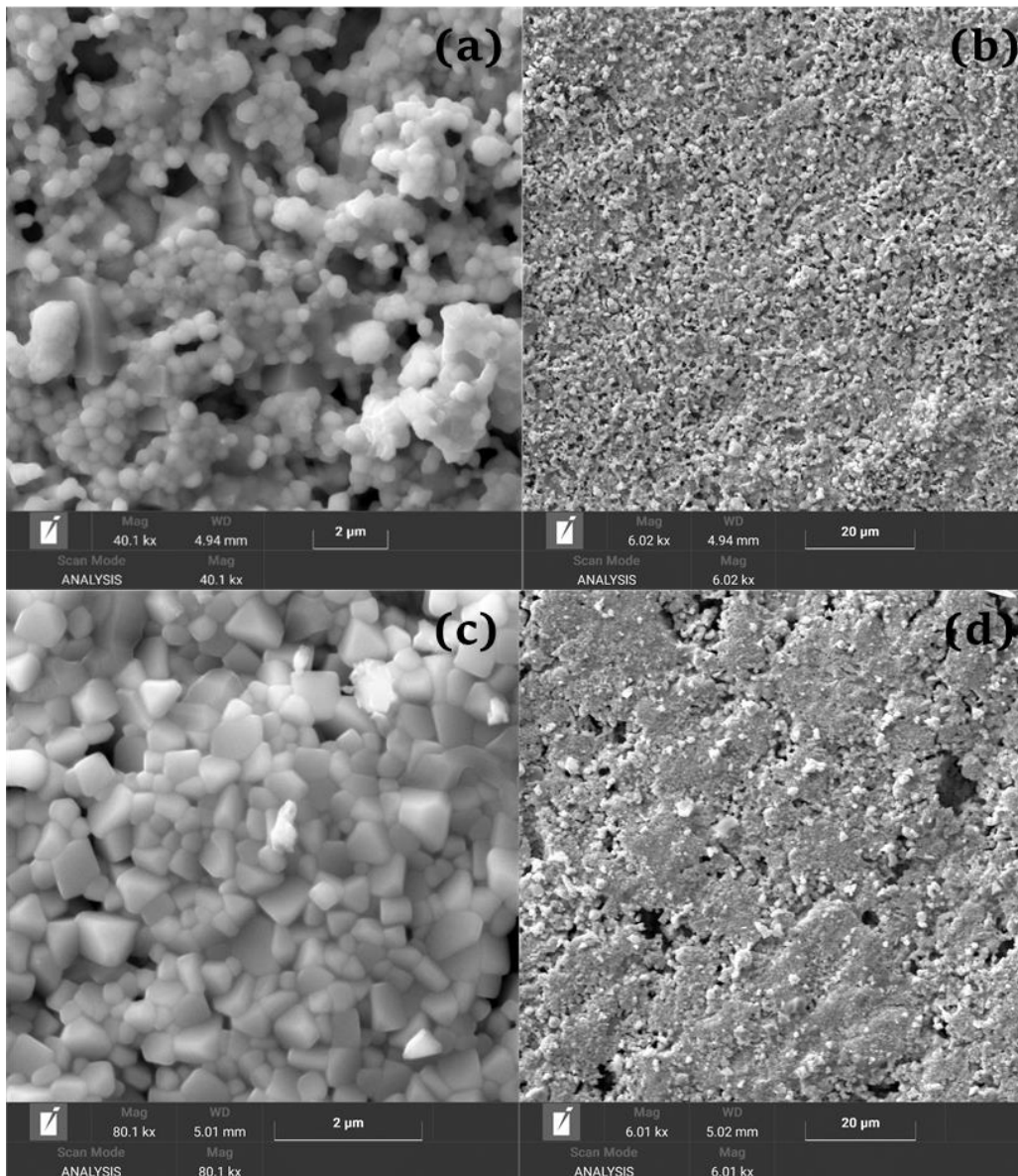**Figure 5** SEM image and element mapping for LWO (a) and LWO$_{RT}$ (b) samples.

| | W M | La L |
|---|---|---|
| Atom% | 11.7 | 88.3 |
| Atomic ratio | 1 | 7.547 |

**Figure 7** SEM images for composites: CLWO (a, b) and CLWO$_{RT}$ (c, d).
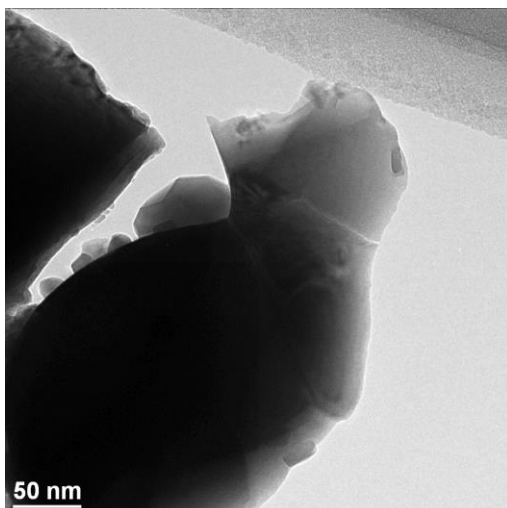


**Figure 8** HR TEM image for CLWO$_{RT}$ sample.
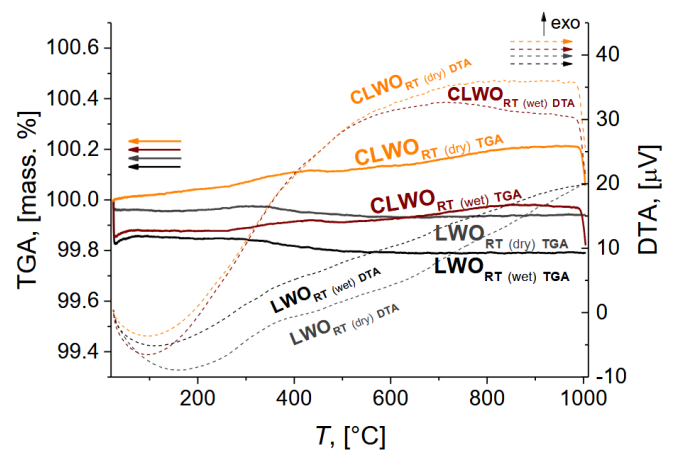


**Figure 9** TGA and DTA curves acquired in dry and wet atmospheres for La$_{27}$W$_5$O$_{55.5-\delta}$ and NiO–CuO–La$_{27}$W$_5$O$_{55.5-\delta}$ samples sintered using electron beam.

For the composite sample the weight loss is not significant, or even the weight gain is observed (Figure 9), perhaps, due to sample reoxidation, demonstrating a poor hydration ability and, hence, probably a low protonic conductivity. It should also be noted that the LNWO perovskite phase may possess poor hydration and proton transport properties compared to the LWO fluorite; however, information on such properties of W-doped La nikelates with perovskite structure is not available in the literature.

## 3.4. Oxygen mobility and surface reactivity

IIE $^{18}O_2$ experiments acquired for the LWO and LWO$_{RT}$ samples at 800 °C are presented in Figures S3a and S4a (Supplementary materials), respectively. As follows from the behavior of $\alpha(t)$ and $f_{16-18}(t)$ curves, the surface exchange is limiting and proceeds predominantly via the R² type of mechanism (Supplementary materials, Figure S1) according to the Muzykantov's classification involving the simultaneous exchange of two oxygen atoms of the oxygen molecule and two oxide anions of the sample surface [51]. According to the analysis of IIE data by non-numerical method [68], $^{18}O$ atomic fractions in the gas phase and in the sample surface are not equilibrated during the majority of the IIE run (Figures S3b and S4b) apparently due to the limitation by the surface exchange process. The oxygen heteroexchange rate ($R$) values at 800 °C calculated by the non-numerical method [68] are $1.6 \cdot 10^{-4}$ mol/(m² s) and $5.1 \cdot 10^{-5}$ mol/(m² s) for the LWO and LWO$_{RT}$ samples, respectively, which corresponds [69] to the oxygen surface exchange constant ($k^*$) values of $2.4 \cdot 10^{-7}$ cm/s and $7.6 \cdot 10^{-8}$ cm/s, respectively.
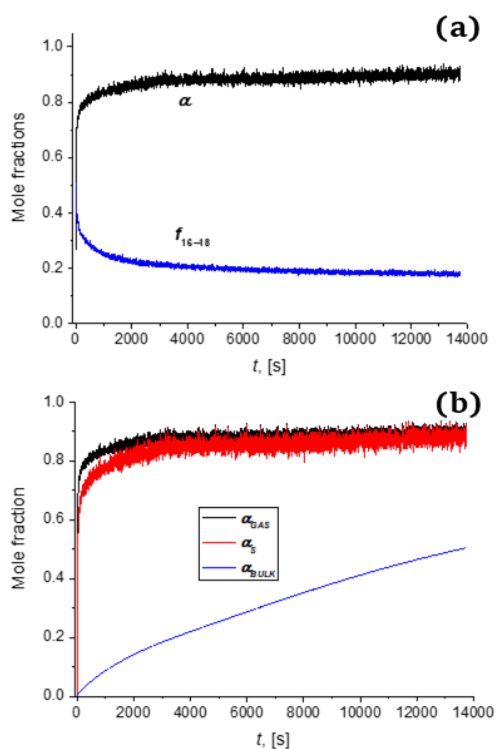


**Figure 10** The experimental time dependencies of $^{18}O$ and $C^{16}O^{18}O$ fractions in the gas phase (a), and $^{18}O$ fraction in the gas phase, on the sample surface and in the sample bulk (b) for LWO sample according to IIE with $C^{18}O_2$ at 320 °C.

IIE $C^{18}O_2$ experiment results acquired for the LWO sample at 320 °C are given in Figure 10a. According to the analysis of the IIE data by the non-numerical method [68], $^{18}O$ atomic fractions in the gas phase and in the sample surface are rapidly equilibrated (Figure 10b); hence, the surface exchange proceeds sufficiently fast to maintain isotopic equilibrium on the samples surface, so the bulk diffusion is limiting. The oxygen tracer diffusion coefficient and surface exchange constant values at 320 °C calculated by the non-numerical method [68] are $4.0 \cdot 10^{-14}$ cm²/s and $1.6 \cdot 10^{-11}$ cm/s, respectively.

The TPIE curves are given in Figure 11. The exchange starts in a low temperature range (~300 °C). ~90% of the overall bulk oxygen is exchanged during TPIE run. The rate of isotope substitution for the LWO$_{RT}$ sample is lower compared to that for the LWO sample. The peak is asymmetric: the bend of the $^{18}O$ atoms fraction curve is sharper at low temperatures. Similar features were observed for Nd tungstates synthesized by mechanical activation and sintered in the furnace [45] and by e-beam [58] and interpreted as an effect of a fast oxygen diffusion along grain boundaries and other extended defects (2D diffusion). 2D diffusion indeed can take place, since grain boundaries are clearly observed (Figure 6). This is in agreement with impedance spectroscopy data for La–W–O samples with differing compositions presented by Magrasó et al. [36]. The data demonstrate the contribution of conductivity along grain boundaries depending on the atmosphere. The other possible reasons for such a behavior to be mentioned are inhibition of the surface exchange at low temperatures and gas diffusion in pores. Inhibition of the oxygen surface exchange resulting in TPIE peak distortion can be associated with the effect of surface carbonates and hydroxyls. On the other hand, such defects as terraces and steps observed by HR TEM (Figure 6) should enhance the oxygen surface exchange. The fast diffusion along open porosity and microcracks of the samples (e.g., similar cracks were detected by TEM, Figure 5b) can take place; however, the oxygen isotope exchange experiment design (using plug flow reactor and using the small granulated samples) should diminish gas phase diffusion limitations effect [59].

The best description can be achieved using the model taking into account an ability of limiting effect of the surface layer permeability on the isotope exchange of oxygen belonging to sample bulk (Figure 12). For this purpose, a parameter $K$, [mol/(cm² s)], an incorporation coefficient, is introduced [70]. This parameter can be denoted as coefficient of permeability or coefficient of mass exchange on the gas – solid phase boundary. The possible physical meaning of the incorporation coefficient ($K$) is the rate of the net process which may include gas transport in pores or voids of the sample and oxygen surface heteroexchange [61, 70, 71]. The calculated parameters are given in Figure 13 and Table 2.

**Table 2** Calculated values of oxygen incorporation coefficient ($K$, [mol/(m² s)]) and tracer diffusion coefficient ($D^*$, [cm²/s]) at 500 °C, their effective activation energy ($E_a$, [kJ/mol]) and fraction of each oxygen form related to the total oxygen content in the material ($\theta$, [%]).

| Sample | Surface mass exchange | | Bulk diffusion | | | | | |
| --- | --- | --- | --- | --- | --- | --- | --- | --- |
| | | | fast | | | slow | | |
| | $K$ | $E_a$ | $D^*$ | $E_a$ | $\theta$ | $D^*$ | $E_a$ | $\theta$ |
| LWO | $1.5 \cdot 10^{-3}$ | 150 | $1.1 \cdot 10^{-11}$ | 50 | 100 | | | |
| LWO$_{RT}$ | $4.6 \cdot 10^{-4}$ | 130 | $2.0 \cdot 10^{-12}$ | 50 | 100 | | | |
| CLWO | | | $2.3 \cdot 10^{-14}$ | 200 | 15 | $5.2 \cdot 10^{-15}$ | 200 | 85 |
| CLWO$_{reox}$ | | | $7.6 \cdot 10^{-13}$ | 100 | 80 | slower | 100 | 20 |

The difference in the incorporation coefficient values for the LWO and LWO$_{RT}$ samples are not significant (Figure 13a) and may be related to the difference in porosity (the smaller pore volume, the higher probability of intra-diffusion retardation) [61, 70, 71]. The same reason can be the one of the factors explaining lower oxygen surface heteroexchange rate value acquired from the IIE $^{18}O_2$ data for the LWO$_{RT}$ sample compared to the for the LWO one.
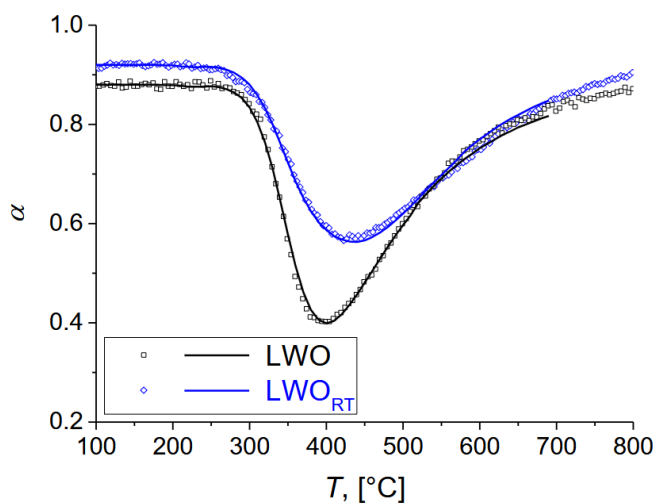


**Figure 11** The temperature dependencies of $^{18}O$ fraction in the gas phase for the LWO and LWO$_{RT}$ samples according to TPIE with $C^{18}O_2$. Points – experiment, lines – modeling.



a – mass exchange between solid and gas    $K$ – incorporation coefficient
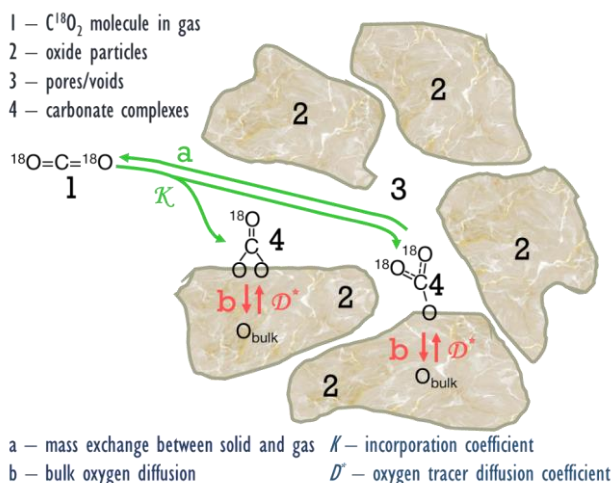b – bulk oxygen diffusion    $D^*$ – oxygen tracer diffusion coefficient

**Figure 12** Schematic illustration of the model of oxygen isotope exchange between $C^{18}O_2$ and oxide.
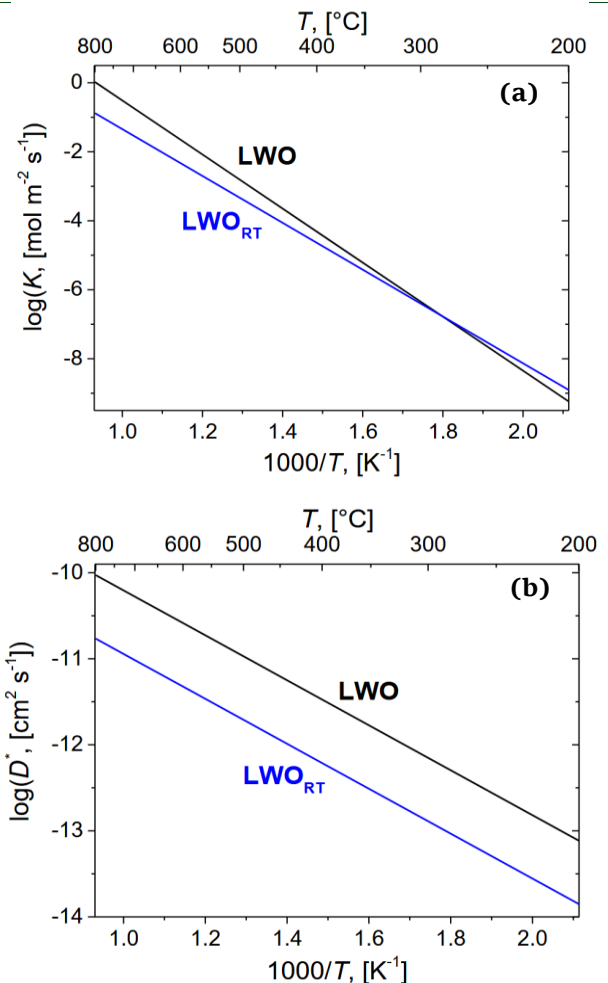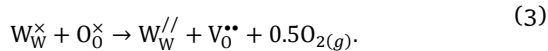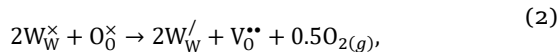




**Figure 13** Arrhenius plots for oxygen incorporation coefficient (a) and tracer diffusion coefficient (b) acquired for the La$_{27}$W$_5$O$_{55.5}$ samples sintered in furnace (LWO) and by RTS (LWO$_{RT}$) from the TPIE $C^{18}O_2$ data.

The values of the oxygen tracer diffusion coefficient for the LWO$_{RT}$ sample are about 5 times lower compared to those for the LWO sample. This is probably related to the different structure disorder level for the conventional and RTS samples due to the effect of e-beam irradiation (Section 3.1). Indeed, the oxygen transport properties of fluorite-like materials are known to demonstrate correlation with the structural disorder [72, 73]. The La:W cation ratio (Table 1) can also affect the oxygen mobility [34, 39, 74–77]. It is modelled that the more W content, the less oxygen vacancy concentration [34, 39, 75]. Moreover, W$^{6+}$

cation can be reduced to form $W^{5+}$ or/and $W^{4+}$ (especially at elevated temperatures and in certain atmospheres), and its reduction to lower valency can result in generating more oxygen vacancies (Equations 2 and 3), causing higher oxygen mobility [52, 78–82]:

$$2W_W^\times + O_O^\times \rightarrow 2W_W^{\prime} + V_O^{\bullet\bullet} + 0.5O_{2(g)}, \tag{2}$$

$$W_W^\times + O_O^\times \rightarrow W_W^{\prime\prime} + V_O^{\bullet\bullet} + 0.5O_{2(g)}. \tag{3}$$

Less W content can result in decreasing the oxygen mobility for this reason as well. Additionally, oxygen vacancies can be more and less ordered depending on the La:W ratio which affects oxygen transport properties [34, 74]. The possible effects of La–O and W–O bond length, oxygen vacancy trapping around W cations and distortion of oxygen local structure can be mentioned for various La:W ratios [73, 74]. Moreover, the grain size and the grain boundary features can affect the oxygen transport as well [31, 32, 36, 45, 58, 76, 77, 83]. The average X-ray scattering region for the LWO$_{RT}$ sample is a few times larger compared to the LWO sample (Table 1) which means larger grain size and less developed grain boundary for the RTS sample as compared with the conventionally sintered sample. This can increase diffusion pathway within grain bulk and decrease oxygen diffusivity along grain boundary, which may lead to the observed decrease in $D^*$ values for the LWO$_{RT}$ sample compared to the LWO one (Figure 13b). Finally, the electron beam damage effects on real/defect structure affecting the oxygen transport properties cannot be fully excluded [54, 77, 84, 85]. Nevertheless, $D^*$ values for the LWO and LWO$_{RT}$ samples remain moderate and are comparable with many other proton-conducting oxides (Supplementary data, Figure S5) [4, 5, 32, 50, 86–92].

Figure 14 demonstrates TPIE results for the CLWO samples. Visually, the rate of oxygen isotope substitution is slower for the CLWO sample compared to that for the LWO sample. There is a hypothesis that such a harsh decline in oxygen diffusivity is related to blocking access of carbon dioxide in the gas phase to fast diffusion pathways of the fluorite phase by adhered particles of Ni (II) or Cu (II) oxides, which has a lower oxide ionic conductivity compared to that for LWO phase [17,36–39]. To provide an access to the fluorite phase surface, such a shield of Ni (II) and Cu (II) oxides should be broken. It can be reached by reduction of the sample by hydrogen (in He + H$_2$ flow at 600 °C for 1 h) (Equation 4):

$$MO + 2 H_2 = M + H_2O, M = Ni, Cu, \tag{4}$$
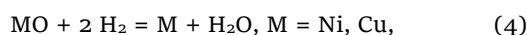
followed by its soft reoxidation (in He + CO$_2$ flow at 800 °C for 1 h) (Equation 5):

$$M + CO_2 = MO + CO, \tag{5}$$
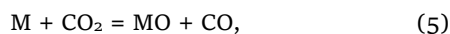
since Ni (II) and Cu (II) oxides and NiCu alloy have different densities. This should cause cracking the NiO+CuO layer leading to a partial release of the fluorite and perovskite particles' surface and, hence, increase its accessibility to CO$_2$ from the gas phase and increase the overall oxygen mobility. Indeed, after reduction and reoxidation, the isotope exchange rate increases significantly (Figures 14, 15); at the same time, nonuniformity of the oxygen substitution rate emerges rather clearly.

There is a lack of information on the effect of Ni and Cu oxides on the oxygen transport properties of their composites with oxide ionic conductive oxides. A drastic decrease in oxygen diffusivity is shown for the composites compared to the initial tungstates, with an increase in oxygen mobility after the reduction and subsequent reoxidation of the composites. This is probably associated with the phase composition features of the composites compared to the initial tungstates (e.g., transformation of initial $Ln_{5.5}(W,Mo)O_{11.25-\delta}$ phase into $Ln_{10}(W,Mo)_2O_{21-\delta}$, $Ln_6(W,Mo)O_{12-\delta}$, etc. with formation of perovskite-like and other admixture phases) as well as blocking the oxygen diffusion by Ni and Cu oxide nanoparticles and partial unblocking of diffusion after reduction and reoxidation.
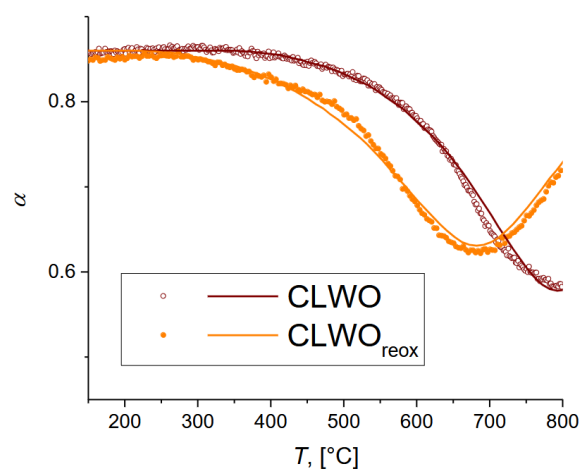


**Figure 14** The temperature dependencies of $^{18}O$ fraction in the gas phase according to TPIE with $C^{18}O_2$ for NiO–CuO–La$_{27}$W$_5$O$_{55.5-\delta}$ samples: initial (CLWO) and after reduction and reoxidation (CLWO$_{reox}$). Points – experiment, lines – modeling.
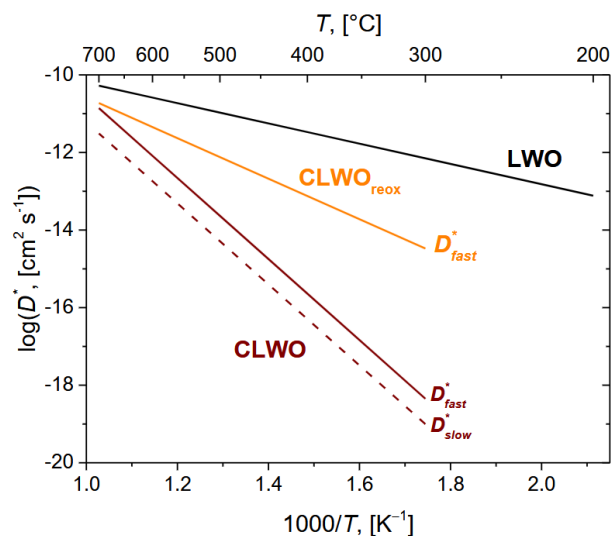


**Figure 15** Temperature dependencies of the oxygen tracer diffusion coefficient according to TPIE with $C^{18}O_2$ data for La$_{27}$W$_5$O$_{55.5-\delta}$ (LWO) and NiO–CuO–La$_{27}$W$_5$O$_{55.5-\delta}$ (CLWO – initial, CLWO$_{reox}$ – after reduction and reoxidation) samples sintered in furnace.

It is to be noted that the diffusion rate is estimated successfully only for the oxygen fraction with a fast substitution due to the nonuniformity and relatively low substitution rate for other channels.

The other possible reason for the difference in oxygen transport characteristics between LWO and CLWO samples to be mentioned is the difference in their phase composition. Firstly, the LWO phase partially transforms into the LNWO perovskite phase in the CLWO composite. This W-doped La nickelate perovskite can affect the oxygen transport characteristics of the composite: as $LaNiO_{3-\delta}$-based perovskite, it can be assumed to possess a high mixed ionic-electronic conductivity [93–95]; however, the effect of doping the Ni site with W on the oxygen mobility has not been studied. Secondly, the $La_6WO_{12-\delta}$-like cubic phase in which oxygen diffusivity may differ due to their structural, defect and redox properties [37–39, 52, 78–82].

## 4. Limitations

The effect of e-beam irradiation on complex oxides and their composites remains poorly understood, particularly in the case of materials based on La tungstates. The assumptions made in this work are based on the experimental data and refer to existing literature, including the authors' previous works. The processing of isothermal isotope exchange data without mathematical modeling provides the effective values of the oxygen tracer diffusion coefficient and the surface exchange constant. These values are useful for developing a more precise mathematical model for processing temperature-programmed isotope exchange data. It should be noted that the isotope exchange data may be interpreted in alternative ways, including as evidence of two-dimensional diffusion or gas-phase diffusion, as discussed in the Results and Discussion section.

## 5. Conclusions

Real and defect structures of La tungstate and its composite with Ni and Cu oxides were studied. The $La_{27}W_5O_{55.5-\delta}$ sample was found to be defective double fluorite, while its composite with NiO+CuO contains perovskite, fluorite, Ni and Cu oxide phases. The presence of extended defects such as grain boundaries, steps/terraces, stacking faults, inclusions etc. was shown. Radiation thermal sintering technique was demonstrated to be promising for obtaining hydrogen separation membranes and their functional layers based on lanthanum tungstate. Lower porosity values compared to conventional sintering at the same temperature are achieved during shorter processing time. The $La_{27}W_5O_{55.5-\delta}$ samples exhibit typical proton conductor properties. According to isotope exchange data, the $La_{27}W_5O_{55.5-\delta}$ samples possess a moderate oxygen mobility, with the diffusion coefficient values being lower for the radiation thermal sintered sample compared to the con-

ventionally sintered one, which is probably due to effect of the structural disordering, La:W cation ratio and grain transport features. For the composite materials, a drastic decrease in the oxygen diffusivity was shown, probably due to the effect of the phase composition as well as blocking the fast diffusion paths by NiO+CuO nanoparticles. Reduction and subsequent reoxidation of the composites result in an increase in the oxygen diffusivity possibly related to a partial unlocking of fast diffusion corresponding to the La tungstate. Hence, good hydration properties and rather high oxygen mobility demonstrated makes the $La_{27}W_5O_{55.5-\delta}$ materials promising for the catalytic membrane reactors, while their composites with NiO+CuO generally comprised of the $LaNi_{0.8}W_{0.2}O_{3-\delta}$ perovskite possessing unknown hydrogen and oxygen transport properties require further studies.

### Author contributions

Conceptualization: Y.B., E.S. (Ekaterina Sadovskaya), V.S.
Data curation: Y.B., E.S. (Ekaterina Sadovskaya), T.K., S.C., E.S. (Evgeny Suprun)
Formal Analysis: N.E., Y.B., E.S. (Ekaterina Sadovskaya), T.K., S.C., E.S. (Evgeny Suprun), A.I.
Funding acquisition: V.S.
Investigation: N.E., Y.B., T.K., S.C., E.S. (Evgeny Suprun), A.I., M.M., M.K.
Methodology: Y.B., E.S. (Ekaterina Sadovskaya), M.M., M.K.
Project administration: V.S.
Supervision: V.S.
Visualization: N.E., Y.B. , E.S. (Ekaterina Sadovskaya), T.K., S.C., E.S. (Evgeny Suprun), A.I.
Writing – original draft: N.E., Y.B., E.S. (Ekaterina Sadovskaya), T.K., S.C.
Writing – review & editing: V.S.

### Conflict of interest

The authors declare no conflict of interest.

### Additional information

Author IDs:

Nikita Eremeev, Scopus ID 55645818400;

Yulia Bespalko, Scopus ID 6505784812, 36450050400;

Ekaterina Sadovskaya, Scopus ID 57202034821, 57204295192;

Tamara Krieger, Scopus ID 8233294600, 57204318584, 57207746128, 57208429063, 57209018046, 57209728104, 57216503916;

Svetlana Cherepanova, Scopus ID 6603228233;

Evgeny Suprun, Scopus ID 26428462300;

Arcady Ishchenko, Scopus ID 57194264619, 57204973965, 57209243975, 57211132956, 57210847860, 57212674271;

Mikhail Mikhailenko, Scopus ID 57283350800;

Mikhail Korobeynikov, Scopus ID 15923261700;

Vladislav Sadykov, Scopus ID 7006677003, 57200684813;

# References

1. Liang W, Zhang Y, Hu T, Jiang H. Enhanced $H_2$ production by using $La_{5.5}WO_{11.25-\delta}$-$La_{0.8}Sr_{0.2}FeO_{3-\delta}$ mixed oxygen ion-proton-electron triple-conducting membrane. Int J Hydrog Energy. 2021;46(66):33143–51. doi:10.1016/j.ijhydene.2021.07.134

2. Cao F, Ji X, Shao Z. Nanotechnologies in ceramic electrochemical cells. Chem Soc Rev. 2024;53(1):450–501. doi:10.1039/D3CS00303E

3. Malavasi L, Karlsson M, Coduri M. Structure-property correlation in oxide-ion and proton conductors for clean energy applications: Recent experimental and computational advancements. J Mater Chem A. 2022;10(10):5082–110. doi:10.1039/D1TA10326A

4. Osinkin D, Tropin E. Hydrogen production from methane and carbon dioxide mixture using all-solid-state electrochemical cell based on a proton-conducting membrane and redox-robust composite electrodes. J Energy Chem. 2022;69:576–84. doi:10.1016/j.jechem.2022.02.019

5. Osinkin DA. Electrochemical behaviour of redox-robust electrode in contact with protonic electrolyte: Case of double-layered $Sr_2Fe_{1.5}Mo_{0.5}O_{6-\delta}$ - $Ce_{0.8}Sm_{0.2}O_{2-\delta}$ composite. Int J Hydrog Energy. 2024;77:1066–73. doi:10.1016/j.ijhydene.2024.06.266

6. Singh M, Paydar S, Singh AK, Singhal R, Singh A, Singh M. Recent advancement of solid oxide fuel cells towards semiconductor membrane fuel cells. Energy Mater. 2024;4:400012. doi:10.20517/energymater.2023.54

7. Plekhanov MS, Thomä SLJ, Zobel M, Cuello GJ, Fischer HE, Raskovalov AA, Kuzmin AV. Correlating proton diffusion in perovskite triple-conducting oxides with local and defect structure. Chem Mater. 2022;34(10):4785–94. doi:10.1021/acs.chemmater.2c01159

8. Saini N, Awasthi K. Insights into the progress of polymeric nano-composite membranes for hydrogen separation and purification in the direction of sustainable energy resources. Sep Purif Technol. 2022;282B:120029. doi:10.1016/j.seppur.2021.120029

9. Alimov VN, Busnyuk AO, Kuzenov SR, Peredistov EU, Livshits AI. Bcc V–Fe alloys for the hydrogen separation membranes: Hydrogen solubility and global character of alloying effect. J Memb Sci. 2022;644:120159. doi:10.1016/j.memsci.2021.120159

10. Singla S, Shetti NP, Basu S, Mondal K, Aminabhavi TM. Hydrogen production technologies – Membrane based separation, storage and challenges. J Environ Manage. 2022;302A:113963. doi:10.1016/j.jenvman.2021.113963

11. Bernardo G, Araújo T, da Silva Lopes T, Sousa J, Mendes A. Recent advances in membrane technologies for hydrogen purification. Int J Hydrog Energy. 2020;45(12):7313–38. doi:10.1016/j.ijhydene.2019.06.162

12. Zhang Q, Liu T, Zhu Z, Hao L, Liu W. Modeling of hydrogen permeation for Ni–ceramic proton conductor composite membrane with symmetric structure. J Memb Sci. 2012;415–16:328–35. doi:10.1016/j.memsci.2012.05.023

13. Poetzsch D, Merkle R, Maier J. Proton conductivity in mixed-conducting BSFZ perovskite from thermogravimetric relaxation. Phys Chem Chem Phys. 2014;16(31):16446–53. doi:10.1039/C4CP00459K

14. Escolástico S, Somacescu S, Serra JM. Tailoring mixed ionic–electronic conduction in $H_2$ permeable membranes based on the system $Nd_{5.5}W_{1-x}Mo_xO_{11.25-\delta}$. J Mater Chem A. 2015;3(2):719–31. doi:10.1039/C4TA03699A

15. Cheng H. Rare earth tungstate: One competitive proton conducting material used for hydrogen separation: A review. Separations. 2023;10(5):317. doi:10.3390/separations10050317

16. Fontaine M, Norby T, Larring Y, Grande T, Bredesen R. Oxygen and hydrogen separation membranes based on dense ceramic conductors. In: Membrane Science and Technology, Volume 13. Elsevier; 2008. pp. 401–58. doi:10.1016/S0927-5193(07)13010-2

17. Bespalko Y, Sadykov V, Eremeev N, Skryabin P, Krieger T, Sadovskaya E, Bobrova L, Uvarov N, Lukashevich A, Krasnov A, Fedorova Y. Synthesis of tungstates/$Ni_{0.5}Cu_{0.5}O$ nanocomposite materials for hydrogen separation cermet membranes. Compos Struct. 2018;202:1263–74. doi:10.1016/j.compstruct.2018.06.004

18. Su H, Hu YH. Degradation issues and stabilization strategies of protonic ceramic electrolysis cells for steam electrolysis. Energy Sci Eng. 2022;10(5):1706–25. doi:10.1002/ese3.1010

19. Shirbhate S, Acharya S. Polyvinyl alcohol/polybenzimidazole/$BaZrO_3$–based hybrid nanocomposite: As a new proton conducting membrane for proton exchange membrane fuel cells. Ferroelectrics. 2022;587(1):118–26. doi:10.1080/00150193.2022.2034421

20. Long Y, Yang K, Gu Z, Lin S, Li D, Zhu X, Wang H, Li K. Hydrogen generation from water splitting over polyfunctional perovskite oxygen carriers by using coke oven gas as reducing agent. Appl Catal B Environ. 2022;301:120778. doi:10.1016/j.apcatb.2021.120778

21. Escolástico S, Solís C, Scherb T, Schumacher G, Serra JM. Hydrogen separation in $La_{5.5}WO_{11.25-\delta}$ membranes. J Memb Sci. 2013;444:276–84. doi:10.1016/j.memsci.2013.05.005

22. Hancke R, Sarah F, Kilner JA, Haugsrud R. Determination of proton- and oxide ion tracer diffusion in lanthanum tungstate (La/W = 5.6) by means of ToF-SIMS. Phys Chem Chem Phys. 2012;14(40):13971–8. doi:10.1039/C2CP42278F

23. Zayas-Rey MJ, dos Santos-Gómez L, Marrero-López D, León-Reina L, Canales-Vázquez J, Aranda MAG, Losilla ER. Structural and conducting features of niobium-doped lanthanum tungsten, $La_{27}(W_{1-x}Nb_x)_5O_{55.55-\delta}$. Chem Mater. 2013;25(3):448–56. doi:10.1021/cm304067d

24. Escolástico S, Vert VB, Serra JM. Preparation and characterization of nanocrystalline mixed proton-electronic conducting materials based on the system $Ln_6WO_{12}$. Chem Mater. 2009;21(14):3079–89. doi:10.1021/cm900067k

25. Baidya A, Dutta A. Exploring phase transition and charge carrier dynamics in $La_6MoO_{12}$ ionic conductors: Impact of metal-substitution. Mater Res Bull. 2024;179:112968. doi:10.1016/j.materresbull.2024.112968

26. Escolástico S, Solís C, Serra JM. Study of hydrogen permeation in $(La_{5/6}Nd_{1/6})_{5.5}WO_{12-\delta}$ membranes. Solid State Ionics. 2012;216:31–5. doi:10.1016/j.ssi.2011.11.004

27. Shlyakhtina A, Lyskov N, Baldin E, Stolbov D, Kolbanev I, Shatov A, Kasyanova A, Medvedev D. Impact of Ln cation on the oxygen ion conductivity of $Ln_{14}W_4O_{33}$ ($Ln$= Nd, Sm, Gd, Dy, Ho, Er, Tm, Yb) tungstates. Ceram Int. 2024;50(1A):704–13. doi:10.1016/j.ceramint.2023.10.149

28. Magrasó A, Haugsrud R. Effects of the La/W ratio and doping on the structure, defect structure, stability and functional properties of proton-conducting lanthanum tungstate $La_{28-x}W_{4+x}O_{54+\delta}$. A review. J Mater Chem A. 2014;2(32):12630–41. doi:10.1039/C4TA00546E

29. Hancke R, Magrasó A, Norby T, Haugsrud R. Hydration of lanthanum tungstate (La/W=5.6 and 5.3) studied by TG and simultaneous TG–DSC. Solid State Ionics. 2013;231:25–9. doi:10.1016/j.ssi.2012.10.022

30. Bespalko Y, Eremeev N, Skryabin P, Krieger T, Chesalov Y, Lapina O, Khabibulin D, Ulihin A, Uvarov N, Sadykov V. Structural and transport properties of neodymium tungstates prepared via mechanochemical activation. Ceram Int. 2019;45(7B):9529–36. doi:10.1016/j.ceramint.2018.09.277

31. Sadykov V, Shlyakhtina A, Sadovskaya E, Eremeev N, Skazka V, Goncharov V. 2D diffusion of oxygen in $Ln_{10}Mo_2O_{21}$ (Ln =

Nd, Ho) oxides. Solid State Ionics. 2020;346:115229. doi:10.1016/j.ssi.2020.115229

32. Shlyakhtina AV, Lyskov NV, Šalkus T, Kežionis A, Patrakeev MV, Leonidov IA, Shcherbakova LG, Chernyak SA, Shefer KI, Sadovskaya EM, Eremeev NF, Sadykov VA. Conductivity and oxygen diffusion in bixbyites and fluorites $Ln_{6-x}MoO_{12-\delta}$ (Ln = Er, Tm; $x$ = 0, 0.5). Int J Hydrog Energy. 2021;46(32):16965–76. doi:10.1016/j.ijhydene.2021.02.029

33. Gilev AR, Kiselev EA, Sukhanov KS, Korona DV, Cherepanov VA. Evaluation of $La_{2-x}(Ca/Sr)_xNi_{1-y}Fe_yO_{4+\delta}$ ($x$= 0.5, 0.6; $y$= 0.4, 0.5) as cathodes for proton-conducting SOFC based on lanthanum tungstate. Electrochim Acta. 2022;421:140479. doi:10.1016/j.electacta.2022.140479

34. Erdal S, Kalland L-E, Hancke R, Polfus J, Haugsrud R, Norby T, Magrasó A. Defect structure and its nomenclature for mixed conducting lanthanum tungstates $La_{28-x}W_{4+x}O_{54+3x/2}$. Int J Hydrog Energy. 2012;37(9):8051–5. doi:10.1016/j.ijhydene.2011.11.093

35. Magrasó A. Transport number measurements and fuel cell testing of undoped and Mo-substituted lanthanum tungstate. J Power Sources. 2013;240:583–8. doi:10.1016/j.jpowsour.2013.04.087

36. Magrasó A, Frontera C, Marrero-López D, Núñez P. New crystal structure and characterization of lanthanum tungstate "$La_6WO_{12}$" prepared by freeze-drying synthesis. Dalton Trans. 2009;46:10273–83. doi:10.1039/B916981B

37. Jayalekshmy NL, John A, Thomas JK, Solomon S. Structural, optical and electrical characterizations of $Ln_6WO_{12}$ (Ln = La, Nd, Sm, Gd) nanoceramics. Appl Phys A. 2019;125(2):143. doi:10.1007/s00339-019-2441-z

38. Polfus JM, Xing W, Fontaine ML, Denonville C, Henriksen PP, Bredesen R. Hydrogen separation membranes based on dense ceramic composites in the $La_{27}W_5O_{55.5}$–$LaCrO_3$ system. J Memb Sci. 2015;479:39–45. doi:10.1016/j.memsci.2015.01.027

39. Partin GS, Korona DV, Neiman AYa, Belova KG. Conductivity and hydration of fluorite-type $La_{6-x}WO_{12-1.5x}$ phases ($x$= 0.4; 0.6; 0.8; 1). Russ J Electrochem. 2015;51(5):381–90. doi:10.1134/S1023193515050092

40. Cao Y, Duan N, Jian L, Evans A, Haugsrud R. Effect of Nb doping on hydration and conductivity of $La_{27}W_5O_{55.5-\delta}$. J Am Ceram Soc. 2016;99(10):3309–16. doi:10.1111/jace.14346

41. Hancke R, Li Z, Haugsrud R. Thermogravimetric relaxation study of the proton conductor lanthanum tungstate, $La_{28-x}W_{4+\delta}O_{54+\delta}v_{2-\delta}$, $x$ = 0.85. Int J Hydrog Energy. 2012;37(9):8043–50. doi:10.1016/j.ijhydene.2011.11.050

42. Surzhikov AP, Malyshev AV, Lysenko EN, Stary O. Temperature dependences of the initial permeability of lithium-titanium ferrites produced by solid-state sintering in thermal and radiation-thermal modes. Eurasian Phys Tech J. 2022;19(1(39)):5–9. doi:10.31489/2022No1/5-9

43. Lyakhov NZ, Boldyrev VV, Voronin AP, Gribkov OS, Bochkarev LG, Rusakov SV, Auslender VL. Electron beam stimulated chemical reaction in solids. J Therm Anal. 1995;43(1):21–31. doi:10.1007/bf02635965

44. Auslender VL, Bochkarev IG, Boldyrev VV, Lyakhov NZ, Voronin AP. Electron beam induced diffusion controlled reaction in solids. Solid State Ionics. 1997;101–3(1):489–93. doi:10.1016/S0167-2738(97)84073-8

45. Eremeev NF, Bespalko YuN, Sadovskaya EM, Skriabin PI, Krieger TA, Ishchenko AV, Sadykov VA. Structural and transport properties of Nd tungstates and their composites with $Ni_{0.5}Cu_{0.5}O$ obtained by mechanical activation. Dalton Trans. 2022;51(19):7705–14. doi:10.1039/d2dt00498d

46. Kostishyn VG, Komlev AS, Korobeynikov MV, Bryazgin AA, Shvedunov VI, Timofeev AV, Mikhailenko MA. Effect of a temperature mode of radiation-thermal sintering the structure and magnetic properties of Mn-Zn-ferrites. J Nano-Electron Phys. 2015;7(4):04044.

47. TOPAS-Academic [Internet]. 2020[Cited 2024]. Available from: http://www.topas-academic.net/, Accessed on 11 December 2024

48. Sadykov V, Sadovskaya E, Bobin A, Kharlamova T, Uvarov N, Ulikhin A, Argirusis C, Sourkouni G, Stathopoulos V. Temperature-programmed $C^{18}O_2$ SSITKA for powders of fast oxide-ion conductors: estimation of oxygen self-diffusion coefficients. Solid State Ionics. 2015;271:69–72. doi:10.1016/j.ssi.2014.11.004

49. Sadykov VA, Sadovskaya EM, Uvarov NF. Methods of isotopic relaxations for estimation of oxygen diffusion coefficients in solid electrolytes and materials with mixed ionic-electronic conductivity. Russ J Electrochem. 2015;51(5):458–67. doi:10.1134/S1023193515050109

50. Sadykov VA, Sadovskaya EM, Eremeev NF, Skriabin PI, Krasnov AV, Bespalko YuN, Pavlova SN, Fedorova YuE, Pikalova EYu, Shlyakhtina AV. Oxygen mobility in the materials for solid oxide fuel cells and catalytic membranes (Review). Russ J Electrochem. 2019;55(8):701–18. doi:10.1134/S1023193519080147

51. Muzykantov VS, Popovski VV, Boreskov GK. Kinetika izotopnogo obmena v sisteme molekulyarnyi kislorod - tvyodyi okisel [Kinetics of isotope exchange in molecular oxygen - solid oxide system]. Kinet Katal. 1964;5(4):624–9. Russian.

52. Seeger J, Ivanova ME, Meulenberg WA, Sebold D, Stöver D, Scherb T, Schumacher G, Escolástico S, Solís C, Serra JM. Synthesis and characterization of nonsubstituted and substituted proton-conducting $La_{6-x}WO_{12-y}$. Inorg Chem. 2013;52(18):10375–86. doi:10.1021/ic401104m

53. Atas MS. The relationship between reinforcement ratio and e-beam irradiation in $Y_2O_3$ reinforced Al6061 alloys: A crystallographic assessment. Nucl Instrum Methods Phys Res B. 2024;548:165252. doi:10.1016/j.nimb.2024.165252

54. Pavlov YuS, Petrenko VV, Alekseev PA, Bystrov PA, Souvorova OA. Trends and opportunities for the development of electron-beam energy-intensive technologies. Radiat Phys Chem. 2022;198:110199. doi:10.1016/j.radphyschem.2022.110199

55. Pikaev A.K. Sovremennaya Radiatsionnaya Khimiya. Osnovnyye Polozheniya, Experimental'naya Tekhnika i Metody [Modern Radiation Chemistr. Basics, Experimental Equipment and Methods]. Moscow: Nauka; 1985. 374 p. Russian.

56. Stepanov VA. Radiation-stimulated diffusion in solids. Tech Phys. 1998;43(8):938–42. doi:10.1134/1.1259104

57. Bespalko Yu, Eremeev N, Sadovskaya E, Krieger T, Bulavchenko O, Suprun E, Mikhailenko M, Korobeynikov M, Sadykov V. Synthesis and oxygen mobility of bismuth cerates and titanates with pyrochlore structure. Membranes. 2023;13(6):598. doi:10.3390/membranes13060598

58. Sadykov V, Bespalko Yu, Sadovskaya E, Krieger T, Belyaev V, Eremeev N, Mikhailenko M, Bryazgin A, Korobeynikov M, Ulihin A, Uvarov N. Structural and transport properties of e-beam sintered lanthanide tungstates and tungstates-molybdates. Nanomater. 2022;12(19):3282. doi:10.3390/nano12193282

59. Sadykov VA, Shlyakhtina AV, Lyskov NV, Sadovskaya EM, Cherepanova SV, Eremeev NF, Skazka VV, Goncharov VB, Kharitonova EP. Oxygen diffusion in Mg-doped Sm and Gd zirconates with pyrochlore structure. Ionics. 2020;26(9):4621–33. doi:10.1007/s11581-020-03614-5

60. Sadykov VA, Bespalko YuN, Pavlova SN, Skriabin PI, Krasnov AV, Eremeev NF, Krieger TA, Sadovskaya EM, Belyaev VD, Vinokurov ZS. Protonic mobility of neodymium tungstate. J Electrochem En Conv Stor. 2017;14(4):044501. doi:10.1115/1.4037957

61. Porotnikova NM, Ananyev MV. Applicability of gas-phase isotope exchange method for investigation of porous materials. J Solid State Electrochem. 2021;25(4):1151–9. doi:10.1007/s10008-020-04896-5

62. Ren R, Sun J, Wang G, Xu C, Qiao J, Sun W, Wang Z, Sun K. Rational design of $Sr_2Fe_{1.5}Mo_{0.4}Y_{0.1}O_{6-\delta}$ oxygen electrode with triple conduction for hydrogen production in protonic ceramic electrolysis cell. Sep Purif Technol. 2022;299:121780. doi:10.1016/j.seppur.2022.121780

63. Kreuer KD. Aspects of the formation and mobility of protonic charge carriers and the stability of perovskite-type oxides.

Solid State Ionics. 1999;125 (1–4):285–302. doi:[10.1016/S0167-2738(99)00188-5](10.1016/S0167-2738(99)00188-5)

64. Farlenkov AS, Vlasov MI, Porotnikova NM, Bobrikov IA, Khodimchuk AV, Ananyev MV. Hydrogen diffusivity in the Sr-doped $LaScO_3$ proton-conducting oxides. Int J Hydrog Energy. 2020;45(43):23455–6810. doi:[10.1016/j.ijhydene.2020.06.148](10.1016/j.ijhydene.2020.06.148)

65. Edwards AG. Measurement of the diffusion rate of hydrogen in nickel. Br J Appl Phys. 1958;8(10):406–10. doi:[10.1088/0508-3443/8/10/306](10.1088/0508-3443/8/10/306)

66. Piper J. Diffusion of hydrogen in copper-palladium alloys. J Appl Phys. 1966;37(2):715–21. doi:[10.1063/1.1708243](10.1063/1.1708243)

67. Huang F, Li X, Shan X, Guo J, Gallucci F. Annaland MVS, Liu D. Hydrogen transport through the V-Cr-Al Alloys: Hydrogen solution, permeation and thermal-stability. Sep Purif Technol 2020;240:116654. doi:[10.1016/j.seppur.2020.116654](10.1016/j.seppur.2020.116654)

68. Sadovskaya EM, Bobin AS, Skazka VV. Isotopic transient analysis of oxygen exchange over oxides. Chem Eng J. 2018;348:1025–36. doi:[10.1016/j.cej.2018.05.027](10.1016/j.cej.2018.05.027)

69. Ananyev MV, Kurumchin EKh, Porotnikova NM. Effect of oxygen nonstoichiometry on kinetics of oxygen exchange and diffusion in lanthanum-strontium cobaltites. Russ J Electrochem. 2010;46(7):789–97. doi:[10.1134/S1023193510070128](10.1134/S1023193510070128)

70. Sadykov V, Eremeev N, Sadovskaya E, Zhulanova T, Pikalov S, Fedorova Yu, Pikalova E. Impact of calcium and copper co-doping on the oxygen transport of layered nickelates: A case study of $Pr_{1.6}Ca_{0.4}Ni_{1-y}Cu_yO_{4+\delta}$ and a comparative analysis. Chim Tech Acta. 2024;11(4): 202411411. doi:[10.15826/chimtech.2024.11.4.11](10.15826/chimtech.2024.11.4.11)

71. Geffroy P-M, Deronzier E, Gillibert J, Munch P, Chartier T, Fouletier J. Determination of oxygen diffusion and surface exchange coefficients of mixed ionic-electronic conductors by oxygen semi-permeation methods. J Electrochem Soc. 2020;167(6):064503. [doi:10.1149/1945-7111/ab7b84](doi:10.1149/1945-7111/ab7b84)

72. Wachsman ED, Boyapati S, Kaufman MJ, Jiang N. Modeling of ordered structures of phase-stabilized cubic bismuth oxides. J Am Ceram Soc. 2000;83(8):1964–8. doi:[10.1111/j.1151-2916.2000.tb01498.x](10.1111/j.1151-2916.2000.tb01498.x)

73. Li Q, Thangadurai V. Synthesis, structure and electrical properties of Mo-doped $CeO_2$–materials for SOFCs. Fuel Cells. 2009;9(5):684–98. doi:[10.1002/fuce.200900044](10.1002/fuce.200900044)

74. Kalland L-E, Magrasó A, Mancini A, Tealdi C, Malavasi L. Local structure of proton-conducting lanthanum tungstate $La_{28-x}W_{4+x}O_{54+\delta}$: A combined density functional theory and pair distribution function study. Chem Mater. 2013;25(11):2378–84. doi:[10.1021/cm401466r](10.1021/cm401466r)

75. Kalland L-EQ. *Ab initio* Modelling and Experimental Studies of Order-Disorder, Hydration, and Ionic Conductivity of Fluorite Related Oxides [PhD Dissertation]. Oslo (Kingdom of Norway): University of Oslo; 2021. 123 p.

76. Baldin E, Lyskov N, Vorobieva G, Kolbanev I, Karyagina O, Stolbov D, Voronkova V, Shlyakhtina A. Synthesis of hexagonal nanophases in the $La_2O_3$–$MO_3$ (M = Mo, W) systems. Energies. 2023;16(15):5637. doi:[10.3390/en16155637](10.3390/en16155637)

77. Zhu Y, Wang J, Rykov AI, Zhu X, Yang W. Oxygen transport kinetics affected by grain size – A permeation model study. J Memb Sci. 2020;603:118038. doi:[10.1016/j.memsci.2020.118038](10.1016/j.memsci.2020.118038)

78. Chen Y, Wei Y, Xie H, Zhuang L, Wang H. Effect of the La/W ratio in lanthanum tungstate on the structure, stability and hydrogen permeation properties. J Memb Sci. 2017;542:300–6. doi:[10.1016/j.memsci.2017.08.031](10.1016/j.memsci.2017.08.031)

79. Amsif M, Magrasó A, Marrero-López D, Ruiz-Morales JC, Canales-Vázquez J, Núñez, P. Mo-substituted lanthanum tungstate $La2_{8-y}W_{4+y}O_{54+\delta}$: A competitive mixed electron–proton conductor for gas separation membrane applications. Chem Mater. 2012;24(20):3868–77. doi:[10.1021/cm301723a](10.1021/cm301723a)

80. Vøllestad E, Gorzkowska-Sobas A, Haugsrud R. Fabrication, structural and electrical characterization of lanthanum tungstate films by pulsed laser deposition. Thin Solid Films. 2012;520(21):6531–4. doi:[10.1016/j.tsf.2012.06.060](10.1016/j.tsf.2012.06.060)

81. Kojo G, Shono Y, Ushiyama H, Oshima Y, Otomo J. Influence of La/W ratio on electrical conductivity of lanthanum tungstate with high La/W ratio. J Solid State Chem. 2017;248:1–8. doi:[10.1016/j.jssc.2017.01.011](10.1016/j.jssc.2017.01.011)

82. Escolástico S, Balaguer M, Solís C, Toldra-Reig F, Somacescu S, Gerhards U, Aguadero A, Haas-Santo K, Dittmeyer R, Serra JM. Promotion of mixed protonic–electronic transport in $La_{5.4}WO_{11.1-\delta}$ membranes under $H_2S$ atmospheres. J Mater Chem A. 2023;11(32):17246–56. doi:[10.1039/d3ta01827j](10.1039/d3ta01827j)

83. De Souza RA, Pietrowski MJ, Anselmi-Tamburini U, Kim S, Munirb ZA, Martin M. Oxygen diffusion in nanocrystalline yttria-stabilized zirconia: The effect of grain boundaries. Phys Chem Chem Phys. 2008;10(15):2067–72. doi:[10.1039/B719363G](10.1039/B719363G)

84. Jiang N. Electron irradiation effects in transmission electron microscopy: Random displacements and collective migrations. Micron. 2023;171:103482. doi:[10.1016/j.micron.2023.103482](10.1016/j.micron.2023.103482)

85. Sadykov VA, Sadovskaya EM, Bespalko YuN, Smal' EA, Eremeev NF, Prosvirin IP, Bulavchenko OA, Mikhailenko MA, Korobeynikov MV. Structural, surface and oxygen transport properties of Sm-doped Nd nickelates. Solid State Ionics. 2024;412:116596. doi:[10.1016/j.ssi.2024.116596](10.1016/j.ssi.2024.116596)

86. Sadykov VA, Bespalko YuN, Krasnov AV, Skriabin PI, Lukashevich AI, Fedorova YuE, Sadovskaya EM, Eremeev NF, Krieger TA, Ishchenko AV, Belyaev VD, Uvarov NF, Ulihin AS, Skovorodin IN. Novel proton-conducting nanocomposites for hydrogen separation membranes. Solid State Ionics. 2018;322:69–78. doi:[10.1016/j.ssi.2018.05.003](10.1016/j.ssi.2018.05.003)

87. Shlyakhtina AV, Pigalskiy KS, Belov DA, Lyskov NV, Kharitonova EP, Kolbanev IV, Borunova AB, Karyagina OK, Sadovskaya EM, Sadykov VA, Eremeev NF. Proton and oxygen ion conductivity in the pyrochlore/fluorite family of $Ln_{2-x}Ca_xScMO_{7-\delta}$ (Ln = La, Sm, Ho, Yb; M = Nb, Ta; $x$ = 0, 0.05, 0.1) niobates and tantalates. Dalton Trans. 2018;47(7):2376–92. doi:[10.1039/c7dt03912c](10.1039/c7dt03912c)

88. Thoréton V, Hu Y, Pirovano C, Capoen E, Nuns N, Mamede AS, Dezanneau G, Yoo CY, Bouwmeester HJM, Vannier RN. Oxygen transport kinetics of the misfit layered oxide $Ca_3Co_4O_{9+\delta}$. J Mater Chem A. 2014;2(46):19717–25. doi:[10.1039/C4TA02198C](10.1039/C4TA02198C)

89. Porotnikova NM, Khodimchuk AV, Zakharov DM, Bogdanovich NM, Osinkin DA. Enhancement of surface exchange and oxygen diffusion of $Sr_{1.95}Fe_{1.4}Ni_{0.1}Mo_{0.5}O_{6-\delta}$ oxide determined by two independent isotope exchange methods. Appl Surf Sci. 2023;613:156015. doi:[10.1016/j.apsusc.2022.156015](10.1016/j.apsusc.2022.156015)

90. Farlenkov AS, Ananyev MV, Eremin VA, Porotnikova NM, Kurumchin EKh, Melekh B-T. Oxygen isotope exchange in doped calcium and barium zirconates. Solid State Ionics. 2016;290:108–15. doi:[10.1016/j.ssi.2016.04.015](10.1016/j.ssi.2016.04.015)

91. De Souza RA, Kilner JA, Jeynes C. The application of secondary ion mass spectrometry (SIMS) to the study of high temperature proton conductors (HTPC). Solid State Ionics. 1997;97(1–4):409–19. doi:[10.1016/S0167-2738(97)00038-6](10.1016/S0167-2738(97)00038-6)

92. Farlenkov AS, Khodimchuk AV, Shevyrev NA, Stroeva AYu, Fetisov AV, Ananyev MV. Oxygen isotope exchange in proton-conducting oxides based on lanthanum scandates. Int J Hydrog Energy. 2019;44(48):26577–88. doi:[10.1016/j.ijhydene.2019.08.088](10.1016/j.ijhydene.2019.08.088)

93. Che W, Wei M, Sang Z, Ou Y, Liu Y, Liu J. Perovskite $LaNiO_{3-\delta}$ oxide as an anion-intercalated pseudocapacitor electrode. J Alloys Compd. 2018;731:381–8. doi:[10.1016/j.jallcom.2017.10.027](10.1016/j.jallcom.2017.10.027)

94. Lu Y, Akbar M, Xia C, Mi Y, Ma L, Wang B, Zhu B. Catalytic membrane with high ion–electron conduction made of strongly correlated perovskite $LaNiO_3$ and $Ce_{0.8}Sm_{0.2}O_{2-\delta}$ for fuel cells. J Catal. 2020;386:117–25. doi:[10.1016/j.jcat.2020.04.004](10.1016/j.jcat.2020.04.004)

95. Alvarez I, Martínez JL, Veiga ML, Pico C. Synthesis, structural characterization, and electronic properties of the $LaNi_{1-x}W_xO_3$ ($0 \le x \le 0.25$) perovskite-like system. J Solid State Chem. 1996;125(1):47–53. doi:[10.1006/jssc.1996.0263](10.1006/jssc.1996.0263)